

**ORBIT DETERMINATION PERFORMANCE IMPROVEMENTS
FOR HIGH AREA-TO-MASS RATIO SPACE OBJECT
TRACKING USING AN ADAPTIVE GAUSSIAN MIXTURES
EXTIMATION ALGORITHM: PREPRINT**

Moriba Jah, et al.

**Boeing LTS Inc.
6200 Uptown Blvd. Suite 240
Albuquerque, NM 87110**

1 July 2009

Technical Paper

APPROVED FOR PUBLIC RELEASE; DISTRIBUTION IS UNLIMITED.



**AIR FORCE RESEARCH LABORATORY
Directed Energy Directorate
3550 Aberdeen Ave SE
AIR FORCE MATERIEL COMMAND
KIRTLAND AIR FORCE BASE, NM 87117-5776**

REPORT DOCUMENTATION PAGE			Form Approved OMB No. 0704-0188		
Public reporting burden for this collection of information is estimated to average 1 hour per response, including the time for reviewing instructions, searching existing data sources, gathering and maintaining the data needed, and completing and reviewing this collection of information. Send comments regarding this burden estimate or any other aspect of this collection of information, including suggestions for reducing this burden to Department of Defense, Washington Headquarters Services, Directorate for Information Operations and Reports (0704-0188), 1215 Jefferson Davis Highway, Suite 1204, Arlington, VA 22202-4302. Respondents should be aware that notwithstanding any other provision of law, no person shall be subject to any penalty for failing to comply with a collection of information if it does not display a currently valid OMB control number. PLEASE DO NOT RETURN YOUR FORM TO THE ABOVE ADDRESS.					
1. REPORT DATE (DD-MM-YYYY) 01-07-2009		2. REPORT TYPE Technical Paper		3. DATES COVERED (From - To) 17 November 2008- 01 July 2009	
4. TITLE AND SUBTITLE Orbit Determination Performance Improvements for High Area-To-Mass Ratio Space Object Tracking Using An Adaptive Gaussian Mixtures Estimation Algorithm: Preprint			5a. CONTRACT NUMBER FA9451-05-C-0257 M124AETIF- 702118		
			5b. GRANT NUMBER		
			5c. PROGRAM ELEMENT NUMBER 60344F		
6. AUTHOR(S) Moriba Jah, Kyle DeMars, Dan Giza, Tom Kelecyc			5d. PROJECT NUMBER 6255		
			5e. TASK NUMBER SM		
			5f. WORK UNIT NUMBER AD		
7. PERFORMING ORGANIZATION NAME(S) AND ADDRESS(ES) Boeing LTS Inc. 6200 Uptown Blvd, Suite 240 Albuquerque, NM 87110			8. PERFORMING ORGANIZATION REPORT NUMBER		
9. SPONSORING / MONITORING AGENCY NAME(S) AND ADDRESS(ES) Air Force Research Laboratory 3550 Aberdeen Ave SE Kirtland AFB, NM 87117-5776			10. SPONSOR/MONITOR'S ACRONYM(S) AFRL/RDSM		
			11. SPONSOR/MONITOR'S REPORT NUMBER(S) AFRL-RD-PS-TP-2009-1023		
12. DISTRIBUTION / AVAILABILITY STATEMENT Approved for public release					
13. SUPPLEMENTARY NOTES Accepted for publication at the 21 st International Symposium for Space Flight Dynamics; Toulouse, France; September 2009. 377ABW-2009-1082; 18 August 2009. "Government Purpose Rights"					
14. ABSTRACT Inactive high area-to-mass ratio (HAMR) resident space objects (RSOs) near the geosynchronous orbit (GEO) regime pose a hazard to active GEO RSOs. The combination of solar radiation pressure (SRP) and solar and lunar gravitational perturbations cause variations in the orbit parameters of the inactive RSOs. The high A/m nature of these objects results in greater sensitivity to the SPR reflected in mean motion, inclination and eccentricity. The subsequent drift with respect to Earth-based tracking sites, combined with a temporal orientation variability with respect to the sun, results in an inability to successfully reacquire many of these RSOs as they transition through periods of days to weeks out of view observing sites. The unknown material properties, approximation in the shadow function used for eclipse modeling, errors in size estimates and variations in the orientation with respect to the sun result in unpredictable (random) errors. The characteristics of the error distributions are of interest, as most commonly used orbit estimation techniques assume a Gaussian distribution. This work examines improvements in the trajectory estimation when applying an approach that attempts to approximate the true probability density function (pdf) of the state error distribution instead of assuming it to be Gaussian. These improvements are evaluated in the context of operation tracking capabilities.					
15. SUBJECT TERMS					
16. SECURITY CLASSIFICATION OF:			17. LIMITATION OF ABSTRACT	18. NUMBER OF PAGES	19a. NAME OF RESPONSIBLE PERSON Moriba Jah
a. REPORT Unclassified	b. ABSTRACT Unclassified	c. THIS PAGE Unclassified			19b. TELEPHONE NUMBER (include area code) 808-875-4500

Standard Form 298 (Rev. 8-98)
Prescribed by ANSI Std. Z39.18

ORBIT DETERMINATION PERFORMANCE IMPROVEMENTS FOR HIGH AREA-TO-MASS RATIO SPACE OBJECT TRACKING USING AN ADAPTIVE GAUSSIAN MIXTURES ESTIMATION ALGORITHM

Kyle DeMars⁽¹⁾, Moriba Jah⁽²⁾, Dan Giza⁽³⁾, Tom Kececy⁽⁴⁾

⁽¹⁾*The University of Texas at Austin, TX 78712, USA*

⁽²⁾*Air Force Research Laboratory, Directed Energy Directorate, Kihei, HI 96753, USA*

⁽³⁾*State University of New York at Buffalo, Buffalo, NY 14260, USA*

⁽⁴⁾*Boeing-LTS, 5555 Tech Center Dr., Colorado Springs, CO 80919, USA
719-638-5388, thomas.m.kececy@boeing.com*

ABSTRACT

Inactive high area-to-mass ratio (HAMR) resident space objects (RSOs) near the geosynchronous orbit (GEO) regime pose a hazard to active GEO RSOs. The combination of solar radiation pressure (SRP) and solar and lunar gravitational perturbations cause variations in the orbit parameters of the inactive RSOs. The high A/m nature of these objects results in greater sensitivity to the SRP reflected in mean motion, inclination and eccentricity. The subsequent drift with respect to Earth-based tracking sites, combined with a temporal orientation variability with respect to the sun, results in an inability to successfully reacquire many of these RSOs as they transition through periods of days to weeks out of view of observing sites. The unknown material properties, approximations in the shadow function used for eclipse modeling, errors in size estimates and variations in the orientation with respect to the sun result in unpredictable (random) errors. The characteristics of the error distributions are of interest, as most commonly used orbit estimation techniques assume a Gaussian distribution. This work examines improvements in the trajectory estimation when applying an approach that attempts to approximate the true probability density function (pdf) of the state error distribution instead of assuming it to be Gaussian. These improvements are evaluated in the context of operational tracking capabilities.

1. BACKGROUND AND GOALS OF THE STUDY

Analysis and simulation results show that the distributions of propagated state errors resulting from each of the observation and modeling uncertainties to be non-Gaussian [1]. Fig. 1. shows the mean total position error distribution for a A/m (AMR) = 10 m²/kg GEO object propagated over 1-day, where the errors include unmodeled rotation, unmodeled atmospheric refraction and absorption of the solar rays during a 1-hour eclipse, a 1% error in the estimated AMR and 1% errors in the specular and diffuse reflection coefficients. The distributions of the position errors from the individual error contributions are shown to be quite different from the total position error distribution only due to AMR state estimation errors, shown in Fig. 2. In summary, the results of the study show that the SRP modeling errors result in the non-Gaussian distribution of position and velocity errors.

Results of recent work [2] show promise when an adaptive Gaussian mixture (AGM) approach is applied to the determination of attitude in the presence of attitude observation and modeling errors. The purpose of this work is to take an initial step towards understanding the utility and possible benefits of implementing an AGM approach to the problem of trajectory estimation given that previous work indicates the tendency of state errors becoming non-Gaussian. Since the AGM methodology is directly aimed at approximating the true state distribution, it is capable of yielding a more realistic

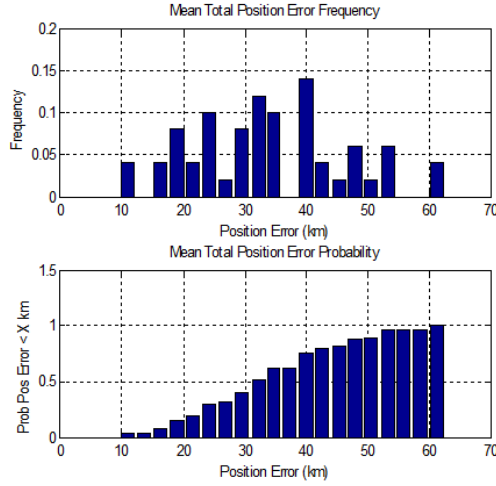


Fig. 1. Total Position Error Distribution for a HAMR GEO Object: Combined Rotation, AMR, Specular and Diffuse Reflection Modeling Errors

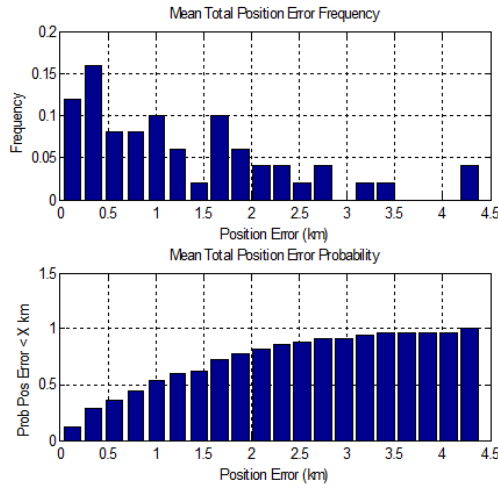


Fig. 2. Total Position Error Distribution for a HAMR GEO Object: AMR Estimation Errors Only

representation of the state distribution. As a consequence, the more realistic state error uncertainties captured by this approach should translate into improved accuracies of subsequent HAMR RSO reacquisition, data/track association, and conjunction assessments.

2. SRP MODELING ERROR INFLUENCE ON HAMR OBJECT ORBIT ERRORS

The analysis presented in this paper examines the state estimation errors resulting from improper modeling of the RSO characteristics. The non-conservative forces affecting RSOs are driven by these characteristics and given that HAMR objects have unknown characteristics *a priori*, the research attempts to assess operational tracking performance in the presence of dynamics mismodeling effects. This tracking performance assessment is done by comparing a method that is constrained to Gaussian assumptions and one that is not. The dynamic models focus on debris objects near the geosynchronous orbit regime having AMR values in the range of $0.1 - 20\text{m}^2/\text{kg}$. The gravitational perturbations are limited to the dominant zonal harmonic (J_2) and luni-solar perturbations since the unknown HAMR dynamic effects are driven solely by non-conservative forces. The sensitivity to SRP modeling errors given by the relatively high AMR values are of interest in assessing the orbital prediction sensitivity to mismodeling of SRP related parameters.

The modeling error analyses are facilitated by comparing trajectories generated via a “truth” model which uses high fidelity force models versus simpler models that are typically used in the reduction and prediction of orbits since there is no method to incorporate a physically realistic model with a lack of *a priori* information. The high fidelity models implement a detailed Earth shadowing model that accounts for atmospheric refraction [3], RSO orientation dependence, and thermal emissions acceleration components that have time-varying material-dependent thermal properties. Lastly, knowledge of the exact AMR value is often poorly known, and so errors attributed to this uncertainty are modeled.

The detailed SRP acceleration model used for this work incorporates both reflective and absorptive effects of the radiation incident on the RSO, in addition to illumination with respect to the sun which is dependent on both Earth eclipsing and RSO orientation changes of the modeled surfaces. The model accommodates any number of specified flat surfaces according to the equations

$$\mathbf{a}_{SRP} = -\frac{1}{c} \sum_{i=1}^{NS} Am_i (F_p \Phi \mathbf{R}_i (\hat{\mathbf{k}}_i \cdot \hat{\mathbf{n}}_i) + \mathbf{P}_i) \quad (1)$$

where the specular and diffuse reflection terms for each surface are defined as

$$\mathbf{R}_i = (1 - s_i) \hat{\mathbf{k}}_i - \frac{2}{3} d_i \hat{\mathbf{n}}_i + 2(\hat{\mathbf{k}}_i \cdot \hat{\mathbf{n}}_i) s_i \hat{\mathbf{n}}_i \quad (2)$$

the emission term is defined as

$$\mathbf{P}_i = \frac{2}{3} a_i \sigma T_i^4 \hat{\mathbf{n}}_i \quad (3)$$

The parameter c is the speed of light, σ is the Steffan-Boltzman constant, and the parameters specific to a surface i are the specular reflectivity coefficient, s_i , the diffuse reflectivity coefficient, d_i , the absorption coefficient, a_i , and the surface temperature T_i . The incident solar flux parameter, Φ , is adjusted according to the distance of the space object from the sun, but has a nominal (average) value of 1367 Watts/m² at distance of 1 Astronomical Unit (AU). The size parameter for each surface is defined as the area to mass ratio $Am_i = A_i/m$ for surface area A_i and mass m . The two unit vectors $\hat{\mathbf{k}}_i$ and $\hat{\mathbf{n}}_i$ represent the incident sun and surface normal, respectively, for surface i . Their dot product defines the attitude dependence of the SRP model. The surface normal unit vectors are defined in a body reference frame, and must be transformed to the inertial reference frame. Finally, the parameter F_p (the shadow function), in the interval $[0, 1]$, is considered in this analysis being that it is the function used to model passage into and out of Earth eclipse. The simplest geometric models are that of a cylinder or a conic/fractional, while the more complex pseudo-physical and physical models attempt to account for the effects of atmospheric refraction and absorption of the incident light rays.

The temperature variations are a function of the illumination angle, the time since shadow entry and its associated illumination angle, and the time since shadow exit as well as its associated illumination angle. Here, the illumination angle is defined as the angle between the incident sun vector and a vector normal (perpendicular) to a given surface. From the radiation pressure modeling work done to support precision orbit determination of the Topex/Poseidon mission [4] the truth trajectory models the temperature variations resulting from the illumination transitions according to assumed materials properties.

3. ESTIMATION STRATEGIES

3.1 Problem formulation

To best understand the innovation presented in this work, we begin with the general formulation of the state model that constitutes the foundation of the orbit determination and prediction process. Consider

the n -dimensional continuous dynamical system described by the differential equation

$$\dot{\mathbf{x}}(t) = \mathbf{f}(t, \mathbf{x}(t)) + \mathbf{G}(t, \mathbf{x}(t))\mathbf{w}(t) \quad (4)$$

where $\mathbf{x}(t) \in \mathbb{R}^n$ is the state vector, $\mathbf{f}(\cdot) \in \mathbb{R}^n$ is the dynamical system model, $\mathbf{w}(t) \in \mathbb{R}^s$ is the dynamical system process noise, and $\mathbf{G}(\cdot) \in \mathbb{R}^{n \times s}$ is a state-dependent shape matrix. The process noise is assumed to be a white-noise process with mean and covariance

$$\mathbb{E}\{\mathbf{w}(t)\} = \mathbf{0} \quad \forall \quad t \quad \text{and} \quad \mathbb{E}\{\mathbf{w}(t)\mathbf{w}^T(\tau)\} = \mathbf{Q}(t)\delta(t - \tau)$$

where $\mathbf{Q}(t) \in \mathbb{R}^{s \times s}$ is the process noise power spectral density and $\delta(t - \tau)$ is the Dirac delta. The continuous dynamical system is accompanied by m -dimensional discrete-time observations described by

$$\mathbf{z}_k = \mathbf{h}(t_k, \mathbf{x}_k) + \mathbf{L}_k \mathbf{v}_k \quad (5)$$

where $\mathbf{z}_k \in \mathbb{R}^m$ is the measurement, $\mathbf{h}(\cdot) \in \mathbb{R}^m$ is the observational model, $\mathbf{v}_k \in \mathbb{R}^r$ is the measurement noise, and $\mathbf{L}_k \in \mathbb{R}^{m \times r}$ is a shape matrix. The measurement noise is assumed to be a white-noise sequence with mean and covariance

$$\mathbb{E}\{\mathbf{v}_k\} = \mathbf{0} \quad \forall \quad k \quad \text{and} \quad \mathbb{E}\{\mathbf{v}_k \mathbf{v}_{k'}^T\} = \mathbf{R}_k \delta_{k,k'}$$

Here, $\delta_{k,k'}$ represents the Kronecker delta.

Given the system described by Eqs. 4 and 5, the goal is to reconstruct the unknown and hidden dynamical process, $\mathbf{x}(t)$, via inference utilizing the observed measurements, \mathbf{z}_k , coupled with the assumed dynamical/observational relationships, $\mathbf{f}(\cdot)$ and $\mathbf{h}(\cdot)$. This goal must be accomplished in the presence of uncertain dynamics with the aid of simultaneous noisy measurements from multiple unknown targets. Therefore, target estimates must be initiated and maintained while simultaneously associating incoming data to existing estimated targets (or classifying the data as belonging to new targets in order to initiate new estimates).

In the context of the problem addressed in this paper, $\mathbf{x}(t)$ is the 6-element vector of Cartesian position and velocity to be estimated in the orbit determination (OD) process, $\mathbf{f}(t, \mathbf{x}(t))$ is the nonlinear model of the forces acting on the object (a function of the state), and $\mathbf{w}(t)$ represents the modeling errors present in the nonlinear forces. Note, the process noise is assumed to be a white noise process, though in reality this is likely not the case. It should also be noted that the SRP coefficient would ideally be a state parameter to be estimated. Though future work will include this, the SRP model error differences incorporated into this analysis serve to address, implicitly, the impact of SRP estimation errors and their associated distributions.

3.2 Track initialization

For any statistically based estimation strategy, a method for obtaining a distribution of the initial state is required. One approach utilized in many orbit determination applications is to perform an initial orbit determination (IOD) step and then refine the initial estimate provided by IOD via a Batch Processor mechanism (e.g. a square-root information filter [5]) before transitioning to sequential estimation (e.g. an extended Kalman filter or an unscented Kalman filter [6, 7]). The classical/standard methods for performing IOD are: Laplace's Method [8], Gauss' Method [8], Double r-Iteration [8], or Gooding's Method [9]. All of the aforementioned IOD methods require the use of measurements comprised of six independent parameters in order to produce a six-parameter orbit. If restrictions are made as to the class of orbits (i.e. removing some of the parameters), the requisite number independent measurement parameters can potentially be reduced. For example, three angle pairs (e.g. right ascension and declination) are typically required for determination of an elliptical (eccentric)

orbit. If, however, we assume the orbit is circular, only two pairs (four independent measurements) are required.

The approach considered here is based on the notion of hypotheses discussed in [10] and assumes an angles-only observational scenario. The utilization of hypotheses for the generation of state estimates allows the bypassing of the IOD state and facilitates the direct entry to sequential estimation. In general, if a measurement of the right ascension and declination of an object is available then four more quantities are required to create a state vector since the state belongs to a six-dimensional space. However, in [10] restricted classes of orbits are considered, allowing for the use of fewer than four quantities in the generation of hypotheses. As a consequence of facilitating a more broad class of orbits, the set of quantities used in hypothesis generation for this work is taken to be: the geocentric range, the velocity magnitude along the radial direction, the velocity magnitude along the tangential direction, and an angle defining the tangential direction.

Briefly, the conversion from measurements and hypotheses to a state is presented. The right ascension, α , and the declination, δ , are made available via an optical observation. Given a hypothesized geocentric range, r , the inertial position of the object with respect to the geocenter is constructed by first forming the unit vectors

$$\mathbf{u}_{stn}^i = \frac{\mathbf{r}_{stn}^i}{\|\mathbf{r}_{stn}^i\|} \quad \text{and} \quad \mathbf{u}_{obj/stn}^i = \begin{bmatrix} \cos \delta \cos \alpha \\ \cos \delta \sin \alpha \\ \sin \delta \end{bmatrix}$$

which represent the unit vector of the observing site with respect to the geocenter and the unit vector of the object with respect to the observing site. The angles γ and β are then computed via

$$\gamma = \pi - \cos^{-1}(\mathbf{u}_{obj/stn}^i \cdot \mathbf{u}_{stn}^i) \quad \text{and} \quad \beta = \pi - \gamma - \sin^{-1}\left(\frac{\|\mathbf{r}_{stn}^i\|}{r} \sin \gamma\right)$$

which facilitates the direct computation of the range from the observing site to the object as

$$\rho = \sqrt{r^2 + \|\mathbf{r}_{stn}^i\|^2 - 2r\|\mathbf{r}_{stn}^i\| \cos \beta}$$

The hypothesized position of the object with respect to the geocenter may then be found to be

$$\mathbf{r}_{obj}^i = \rho \mathbf{u}_{obs/stn}^i + \mathbf{r}_{stn}^i \quad (6)$$

Now, using the hypothesized object position and the hypothesized angle defining the tangential direction (i.e. θ), the unit vector pointing to the object with respect to the geocenter and a rotation matrix are computed as

$$\mathbf{u}_r = \frac{\mathbf{r}_{obj}^i}{\|\mathbf{r}_{obj}^i\|} \quad \text{and} \quad \mathbf{T} = \mathbf{I}_{3 \times 3} - \sin \theta [\mathbf{u}_r \times] + (1 - \cos \theta) [\mathbf{u}_r \times]^2$$

where $\mathbf{I}_{3 \times 3}$ represents the identity matrix of square dimension three and $[\cdot \times]$ represents the skew-symmetric matrix resulting from the vector. \mathbf{T} is a rotation by angle θ about axis \mathbf{u}_r , which represents the orientation of the tangential (in-track) direction and is bounded by the orbit inclination. The hypothesized in-track unit vector is then given by

$$\mathbf{u}_i = \mathbf{T} \frac{\mathbf{e}_3 \times \mathbf{u}_r}{\|\mathbf{e}_3 \times \mathbf{u}_r\|}$$

where $\mathbf{e}_3 \in \mathbb{R}^3$ has the third element to be unity and the remaining elements to be zero. In the case where $bme_3 = \mathbf{u}_r$, another unit vector can be used in place of \mathbf{e}_3 without loss of generality. Finally,

the hypothesized velocity of the object with respect to the geocenter may be computed making use of the hypothesized radial velocity, v_r , and the hypothesized tangential velocity, v_θ , as follows

$$\mathbf{v}_{obj}^i = v_r \mathbf{u}_r + v_\theta \mathbf{u}_i \quad (7)$$

Therefore, given the measurement data as α and δ and the hypothesis data as r , θ , v_r , and v_θ , a hypothesized position and velocity, i.e. Eqs. 6 and 7, of the object with respect to the geocenter may be determined. This process is repeated for each combination of hypotheses.

3.3 Multiple hypothesis filter

The multiple hypothesis filter (MHF) is essentially a bank of UKF filters which are weighted based on the time-history statistical agreement to incoming data. The initial bank of filters is initiated by transforming each hypothesis into a state mean and covariance via the unscented transform [7] which allows the measurement uncertainty and uncertainty associated with the hypothesis selection to be transformed into state uncertainty. The filters are initialized with equal weights. As more data are processed, the MHF recursively refines the available hypotheses, updating the filter weights and pruning hypotheses which have not agreed to acquired data. When one hypothesis dominates, the MHF becomes equivalent to a single UKF, making it a winner-take-all method. However, it is also possible that multiple hypotheses are consistent with the collected data due to the existence of multiple local minima or a geometry-induced lack of observability, or that more than one hypothesis converges to the same local (or global) minimum. More specific information on the MHF methodology and its implementation can be found in [10].

3.4 Adaptive Gaussian mixtures

At the end of a measurement track, the MHF algorithm is typically left with one or two Gaussian hypotheses that propagate to the next measurement using an unscented Kalman filter to maintain the mean and covariance. The AGM methodology attempts to characterize the time evolution of a state probability density function (pdf), rather than a simple mean and covariance, by assuming that the distribution can be represented by a finite sum of Gaussian components. These components are chosen based on the hypotheses after they are conditioned by measurements. For stochastic continuous dynamic systems, the exact evolution of the state pdf is given by the Fokker-Planck-Kolmogorov (FPK) equation [11, 12],

$$\frac{\partial}{\partial t} p(t, \mathbf{x}(t)) = \mathbf{f}^T(t, \mathbf{x}(t)) \frac{\partial p(t, \mathbf{x}(t))}{\partial \mathbf{x}(t)} + \frac{1}{2} \text{trace} \left\{ \mathbf{G}(t, \mathbf{x}(t)) \mathbf{Q}(t) \mathbf{G}^T(t, \mathbf{x}(t)) \frac{\partial^2 p(t, \mathbf{x}(t))}{\partial \mathbf{x}(t) \partial \mathbf{x}(t)^T} \right\} \quad (8)$$

which is a formidable problem to solve because of the following issues:

- *Positivity* of the pdf: $p(t, \mathbf{x}) d\mathbf{x} \geq 0$.
- *Normalization* constraint of the pdf: $\int_{\mathbb{R}^n} p(t, \mathbf{x}) d\mathbf{x} = 1$.
- *No fixed Solution Domain*: how to impose boundary conditions in a finite region and restrict numerical computations.

Note that in Eq. 8 and in the following developments, the derivative of a scalar with respect to a vector has been taken to be a column vector and not a row vector. Analytical solutions to the FPK equation are restricted to a limited class of dynamic systems, and numerical methods suffer in higher dimension systems. Approximating the forecast state pdf using a finite Gaussian mixture model offers a way to impose the aforementioned restrictions on the solution of the FPK equation, and leads to a convex quadratic programming problem for which straightforward solutions exist.

Consider the following equation depicting the Gaussian mixture model approximation for the forecast conditional density function, $p(t, \mathbf{x}(t) | \mathbf{Z}_k)$

$$\hat{p}(t, \mathbf{x}(t) | \mathbf{Z}_k) = \sum_{i=1}^N w_{t|k}^i p_i \quad \text{with} \quad p_i = \mathcal{N}(\mathbf{x}(t) | \boldsymbol{\mu}_{t|k}^i, \mathbf{P}_{t|k}^i) \quad (9)$$

Here, $\boldsymbol{\mu}_{t|k}^i$ and $\mathbf{P}_{t|k}^i$ represent the conditional mean and covariance of the i^{th} component of the Gaussian mixture pdf with respect to the k measurements, and $w_{t|k}^i$ denotes the amplitude of i^{th} Gaussian in the mixture. Furthermore, $\mathcal{N}(\mathbf{x} | \boldsymbol{\mu}, \mathbf{P})$ represents the calculation of a Gaussian probability density function for the random variable \mathbf{x} with mean $\boldsymbol{\mu}$ and covariance \mathbf{P} , i.e.

$$\mathcal{N}(\mathbf{x} | \boldsymbol{\mu}, \mathbf{P}) = \frac{1}{\sqrt{|2\pi\mathbf{P}|}} \exp\left(-\frac{1}{2}(\mathbf{x} - \boldsymbol{\mu})^T \mathbf{P}^{-1}(\mathbf{x} - \boldsymbol{\mu})\right)$$

The positivity and normalization constraints on the mixture pdf, $\hat{p}(t, \mathbf{x}(t) | \mathbf{Z}_k)$, lead to constraints on the amplitudes as

$$\sum_{i=1}^N w_{t|k}^i = 1 \quad \text{and} \quad w_{t|k}^i \geq 0 \quad \forall t \quad (10)$$

In [13], it is shown that since all the components of the mixture pdf of Eq. 9 are Gaussian, only estimates of their mean and covariance need to be maintained between t_k and t_{k+1} in order to obtain the optimal state estimates. These can be propagated by using a continuous-time derivation of the unscented Kalman filter [6, 14], which uses a set of deterministically chosen sigma-points that capture the mean and covariance of the initial distribution.

Notice that the weights w_i corresponding to each Gaussian component are also unknown. Hence, the idea is to use FPK equation error as a feedback to update the amplitude of different Gaussian components in the mixture pdf. In other words, we seek to minimize the FPK equation error under the assumption of Eqs. 9 and 10. Substituting Eq. 9 in Eq. 8 leads to

$$e(t, \mathbf{x}(t)) = \frac{\partial \hat{p}(t, \mathbf{x}(t) | \mathbf{Z}_k)}{\partial t} - \mathcal{L}_{FPK}(\hat{p}(t, \mathbf{x}(t) | \mathbf{Z}_k)) \quad (11)$$

where $\mathcal{L}_{FPK}(\cdot)$ is the FPK operator. The application of this operator is given by,

$$\mathcal{L}_{FPK}(\hat{p}(t, \mathbf{x}(t) | \mathbf{Z}_k)) = \sum_{i=1}^N w_{t|k}^i \mathcal{L}_{FPK}(p_i) \quad (12)$$

with the application of the FPK operator to the individual Gaussian components given by

$$\begin{aligned} \mathcal{L}_{FPK}(p_i) = & - \left(\frac{\partial p_i}{\partial \mathbf{x}(t)} \right)^T \mathbf{f}(t, \mathbf{x}(t)) - p_i \text{trace} \left\{ \frac{\partial \mathbf{f}(t, \mathbf{x}(t))}{\partial \mathbf{x}(t)} \right\} \\ & + \frac{1}{2} \text{trace} \left\{ \mathbf{Q}(t) \frac{\partial^2 p_i}{\partial \mathbf{x}(t) \partial \mathbf{x}(t)^T} \right\} \end{aligned} \quad (13)$$

The first term in Eq. 11 is the time derivative of the probability density function approximated by the Gaussian mixture, and is given by,

$$\frac{\partial \hat{p}(t, \mathbf{x}(t) | \mathbf{Z}_k)}{\partial t} = \sum_{i=1}^N \left[\dot{w}_{t|k}^i p_i + w_{t|k}^i \left(\frac{\partial p_i}{\partial \boldsymbol{\mu}_{t|k}^i} \right)^T \dot{\boldsymbol{\mu}}_{t|k}^i + w_{t|k}^i \text{trace} \left\{ \frac{\partial p_i}{\partial \mathbf{P}_{t|k}^i} \dot{\mathbf{P}}_{t|k}^i \right\} \right] \quad (14)$$

The derivatives of the first two moments are given by UKF equations [14], and the derivative of the weights, \dot{w}_i , is obtained by the following finite difference approach:

$$\dot{w}_{t|k}^i = \frac{1}{\Delta t} (w_{t'|k}^i - w_{t|k}^i) \quad \text{where} \quad t' = t + \Delta t \quad (15)$$

One point of interest is the computation of tangent linear dynamics (the dynamics Jacobian) required for use in Eq. 13, i.e. the computation of

$$\mathbf{F}(t, \mathbf{x}(t)) = \frac{\partial \mathbf{f}(t, \mathbf{x}(t))}{\partial \mathbf{x}(t)}$$

Since the UKF is being utilized, the tangent linear dynamics matrix is not directly available and a method for approximating this matrix must be employed. Consider the cross-covariance between the state and the dynamics of the state, represented by $\mathbf{P}_{x\dot{x}}$. In the case of linear dynamics with respect to the state, the cross-covariance may be computed as

$$\mathbf{P}_{x\dot{x}} = \mathbf{P}_x \mathbf{F}^T(t, \mathbf{x}(t))$$

which implies that if the covariance on the state is known and the cross-covariance between the state and the dynamics is known, then the tangent linear dynamics may be approximated as

$$\mathbf{F}(t, \mathbf{x}(t)) = \mathbf{P}_{x\dot{x}}^T \mathbf{P}_x^{-1}$$

Utilizing the UKF, the cross-covariance is found to be

$$\mathbf{P}_{x\dot{x}} = \sum_{i=0}^{2n} w_i^{(c)} (\mathbf{x}_i - \mathbf{m}_x)(\dot{\mathbf{x}}_i - \mathbf{m}_{\dot{x}})^T$$

where n is the dimension of the state, $w_i^{(c)}$ are covariance weights [14], \mathbf{x}_i are the sigma-points, \mathbf{m}_x is the mean value of \mathbf{x} , $\dot{\mathbf{x}}_i$ are the transformed sigma-points given by evaluating the dynamical system at each of the sigma-points, and $\mathbf{m}_{\dot{x}}$ is the mean value of the transformed sigma-points. Thus, implementing a UKF structure, the tangent linear dynamics matrix can be approximated and applied to Eq. 13.

Now, at a given instant in time after propagating the mean and covariance of each Gaussian component, we seek to update the weights of the Gaussian mixture model by minimizing Eq. 11 over the volume of interest. This requires the computation of several integrals that lead to a convex quadratic programming problem with a unique solution, of which the full derivation can be found in [15]. Using this formulation, one can approximate the time-evolution of the conditional state-pdf at any time instant.

A major challenge in solving the convex minimization problem, however, is the need to evaluate integrals involving Gaussian pdfs over volume V . This volume V can be defined making use of the approximation that the mass of a Gaussian pdf is concentrated in a finite volume around its mean. This is one of the major advantages of using Gaussian mixture models, because the space over which probability mass lies is easy to define. The full derivation of these integrals can be found in [15], and they can be computed exactly for polynomial nonlinearity. In general, numerical integration methods are necessary such as Gaussian quadrature, Monte Carlo integration or unscented transformation [16]. While in lower dimensions the unscented transformation and Gaussian quadrature methods are mostly equivalent, the unscented transformation is computationally more appealing in higher dimensions because the number of points taken to evaluate the integral grows only linearly with the number of dimensions.

3.5 Probabilistic data association

In situations involving simultaneous measurements of multiple targets, association of the incoming data to existing tracks is an integral step in computing accurate solutions. There are many data association schemes discussed in the literature; however, the method used in this work is the probabilistic data association method (PDA).

The method employs a statistical generalization of the typical Euclidean distance, termed the Mahalanobis distance, which is computed by

$$d^2 = (z_k - \hat{z}_k^-)^T P_z^{-1} (z_k - \hat{z}_k^-)$$

where z_k is the incoming measurement data, \hat{z}_k^- is the predicted value of the measurement data, and P_z is the covariance of the difference between the incoming and predicted measurement data (i.e. the innovations covariance). It can be shown that for Gaussian distributions the Mahalanobis distance satisfies a χ^2 distribution. Specification of a probability gate can then be used to validate/associate (or can also be thought of as a scheme to reject) measurements with a χ^2 distribution table. However, if several measurements are validated/associated, then there exists a *hard decision*. That is, it must be decided which measurement(s) to associate and which measurement(s) to reject.

The PDA method [17] offers a data association solution which avoids the need to make a hard decision and instead fuses all relevant information based on statistical agreement. Given m available measurements at time t_k , the measurements are determined to be valid if their computed Mahalanobis distance falls below some threshold dictated by a probability gate [17]. The number of validated measurements, v , is such that $v \leq m$. For each of the associated measurements, the association event probabilities are calculated as

$$\alpha_i = \frac{\mathcal{N}(z_k^i | \hat{z}_k^{i,-}, P_z^i)}{\sum_{j=1}^v \mathcal{N}(z_k^j | \hat{z}_k^{j,-}, P_z^j)} \quad \text{such that} \quad \sum_{i=1}^v \alpha_i = 1$$

The association event probabilities describe how likely it is that a validated measurement actually originated from the target under consideration. Once the association event probabilities have been determined, each of the validated measurements may be processed to produce an updated distribution, which is computed as a mixture of the individual updates from each validated measurement [10, 17].

4. SIMULATION AND ANALYSIS RESULTS

4.1 Simulation description

The overall simulation environment consists of modules which initialize HAMR objects according to input distribution characteristics for the orbit, object shape, and material properties, integrate the HAMR objects over a specified period of time, simulate measurements of right-ascension and declination, and then apply estimation strategies to attempt to recover the object's orbit. To integrate the HAMR objects over a period of time, a high-fidelity model accounting for the accelerations due to gravity (point-mass, zonal harmonics, and/or spherical harmonics), third body perturbations accounting for accurate positioning of the bodies (especially solar and lunar perturbation), and solar radiation pressure with attitude-dependent and thermal radiation effects is applied. In generating the simulated measurements, methods for the accounting for observer lighting conditions, target object lighting conditions, light-time transit delay [18], stellar aberration effects [19], and sensor field-of-view limitations are employed. Furthermore, a specified distribution for a measurement bias and a noise are sampled to add corruption to the measurements. In addition, a Monte Carlo capability is implemented to generate different measurement sequences by sampling the measurement bias and noise distributions on each run. This capability provides a mechanism for generating filtering solutions for many different measurement sequences as a way of testing robustness to the measurements.

The measurement availability for the scenario considered is summarized by: an initial tracking segment of 15 minutes with measurements every 30 seconds, a data gap lasting 6 hours, a final tracking segment of 15 minutes with measurements every 30 seconds, and a final data gap lasting 17.5 hours. The measurements utilized are topocentric right ascension and declination from a station with a known location with each angle measurement having a zero-mean random constant bias with a standard deviation of 0.5 arc-seconds and a zero-mean random noise with a standard deviation of 1 arc-second.

4.2 Orbit and parameter distributions

In the analysis, a truth reference orbit is generated via numerical integration with specified orbit parameter (Keplerian element) distributions for the initial conditions of the integrator and by specification of SRP-related material properties. The Keplerian element distributions considered for the analysis are all uniform distributions with specified minimum/maximum parameter values, which are taken to be

$$\begin{aligned} 38,000 \text{ [km]} \leq a \leq 43,000 \text{ [km]}, \quad 0 \leq e \leq 0.4, \quad 0 \text{ [deg]} \leq i \leq 10 \text{ [deg]} \\ 0 \text{ [deg]} \leq \Omega \leq 360 \text{ [deg]}, \quad 0 \text{ [deg]} \leq \omega \leq 360 \text{ [deg]}, \quad \text{and} \quad 0 \text{ [deg]} \leq M \leq 360 \text{ [deg]} \end{aligned}$$

where a is the semi-major axis, e is the eccentricity, i is the inclination, Ω is the right-ascension of the ascending node, ω is the argument of perigee, and M is the mean anomaly. The material properties are generated by randomly selecting a material with a 60% probability of the material being end-of-life (EOL) MLI Kapton, a 30% probability of the material being solar cells, and a 10% probability of the material being EOL white paint. The selection of the material then determines the diffuse reflectance, d , and the specular reflectance, s . The values used in this analysis are [20]

$$\begin{aligned} \text{EOL MLI kapton : } d &= 0.03 \quad \text{and} \quad s = 0.35 \\ \text{solar cells : } d &= 0.04 \quad \text{and} \quad s = 0.04 \\ \text{EOL white paint : } d &= 0.53 \quad \text{and} \quad s = 0.03 \end{aligned}$$

In all cases, the absorption, a , is chosen so that the three material property values sum to unity, i.e. $a + d + s = 1$. Finally, the area-to-mass ratio is selected randomly using a uniform distribution with specified minimum/maximum value, which are taken to be

$$0.1 \text{ [m}^2\text{/kg]} \leq \frac{A}{m} \leq 20 \text{ [m}^2\text{/kg]}$$

4.3 MHF and AGM results comparison

A Monte Carlo analysis sampling the measurement bias and noise distributions on each run was performed for the MHF algorithm. The estimation errors and the associated 3σ estimation error covariances are shown in radial, in-track, and cross-track (RIC) coordinates in Fig. 3. and Fig. 4. In both figures, the consistent behavior of the MHF is clearly demonstrated. The algorithm is consistently able to initiate the state estimate, refine that initial estimate, reacquire the object after a period of no data, and then forward predict the state estimates. However, it is also seen that the collection of Monte Carlo runs is not very representative of the filter's perception of the estimation errors with clearly present biases and non-normal behavior. Furthermore, it can be seen in Fig. 4. that at some point during the simulation run, the estimation error from every Monte Carlo run strays beyond the 3σ covariance bound of the filter, indicating that the filter is not properly capturing the behavior of the estimation error.

Since the PDA method for data association relies on an accurate accounting of the state estimation errors in order to properly gate and accept/reject measurement data, it is possible that the MHF will

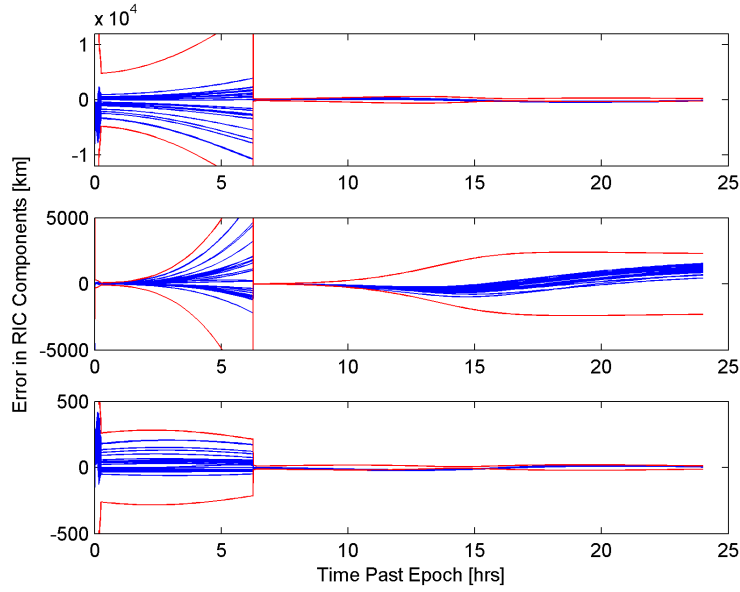


Fig. 3. Estimation error of Monte Carlo runs for the MHF algorithm for the full 24 hours of the simulation. Estimation error is in blue and the 3σ estimation error covariance is shown in red.

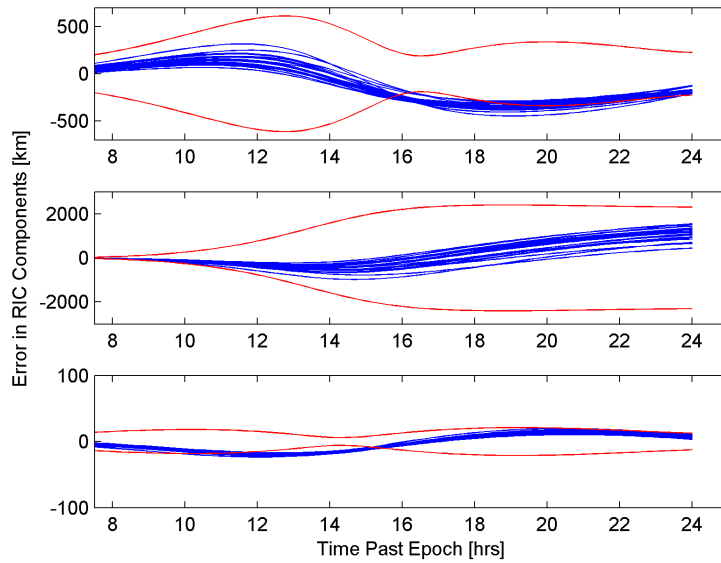


Fig. 4. Estimation error of Monte Carlo runs for the MHF algorithm for the time period starting after the end of the second measurement arc. Estimation error is in blue and the 3σ estimation error covariance is shown in red.

fall into a situation in which measurements become consistently rejected. This can be clearly seen from Fig. 4. at 14 hours past epoch in the cross-track component where all of the samples are outside of the 3σ covariance bound. An attempt to reacquire the object at this time would result in a failure of the algorithm to properly associate data due to the misrepresentation of the state uncertainty by the MHF. To help solve this problem, an AGM was implemented in an attempt to better characterize the state estimation errors. The MHF and AGM methods were applied to a single-run case in order to demonstrate the relative performance of the two algorithms. The RIC state estimation errors and the associated filter covariances for the two methods are shown in Fig. 5. and Fig. 6. It is seen, especially

in Fig. 6. that the state estimation errors for the two methods are comparable; however, the major difference lies in the difference between each filter's perception of the potential distribution of the errors. That is, the AGM 3σ covariance is sufficient enough to encompass the estimation error at the points where the MHF 3σ covariance does not encompass the MHF estimation error. As previously mentioned, this is a particularly important aspect in the association of measurement data to existing estimates. With a more proper representation of the state estimation error distribution data association can function more appropriately, which would lead to a better reacquisition of objects.

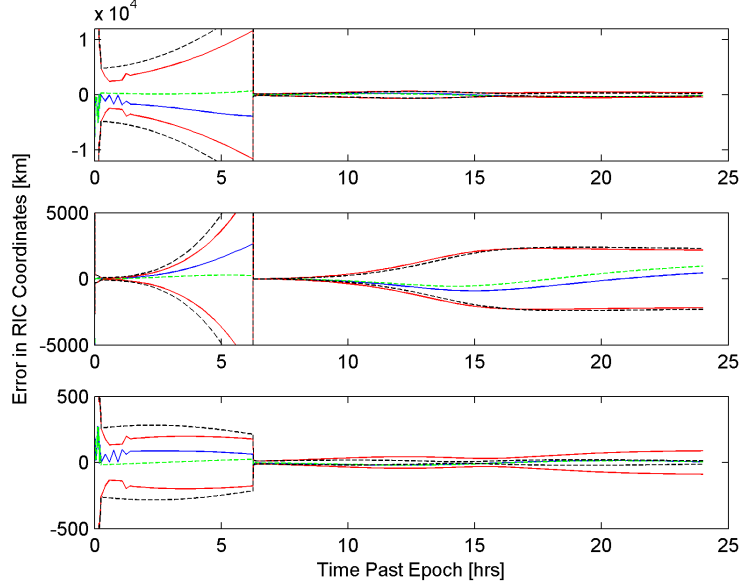


Fig. 5. Estimation error for the MHF and AGM algorithms for the full 24 hours of the simulation. Estimation error for the AGM is in solid blue and for the MHF is in dashed green. The 3σ estimation error covariance for the AGM is in solid red and for the MHF is in dashed black.

Finally, to compare the measurement prediction at the end of the time span, contours of constant probability were computed for both the MHF and AGM method. These are plotted for two different probability values in Fig. 7. Along with the contours, the true measurement as well as the prediction of the measurement value for the MHF and the AGM are plotted for comparison. The curves of constant probability are computed by taking the peak value of the pdf for each method and determining the locus of points corresponding to a scaled value of this peak probability, i.e. 50% of the peak in Fig. 7(a). and 1% of the peak in Fig. 7(b). The percentage of peak probability corresponds to confidence intervals with the smaller percentage corresponding to a larger confidence region. That is, in defining an area upon which to search for the object, the area defined by a 50% peak is going to be smaller than the area defined by a 1% peak. From Fig. 7(a)., it can be seen that for the 50% contour, the MHF contour does not encompass the true measurement while the AGM contour does encompass the true measurement. In the case of a 1% contour, both methods have contours encompassing the true measurement. In both figures, it is clearly seen that the AGM prediction of the measurement is closer than that of the MHF. Ultimately, the fact that a contour corresponding to a larger percentage of peak probability encompasses the result means that a smaller relative area can be searched in an attempt to locate a previously tracked HAMR RSO.

5. CONCLUSIONS AND FUTURE WORK

Monte Carlo analysis of an MHF method applied to the initialization, tracking, and prediction of a HAMR object has been illustrated and shown to exhibit non-Gaussian behaviors and the potential

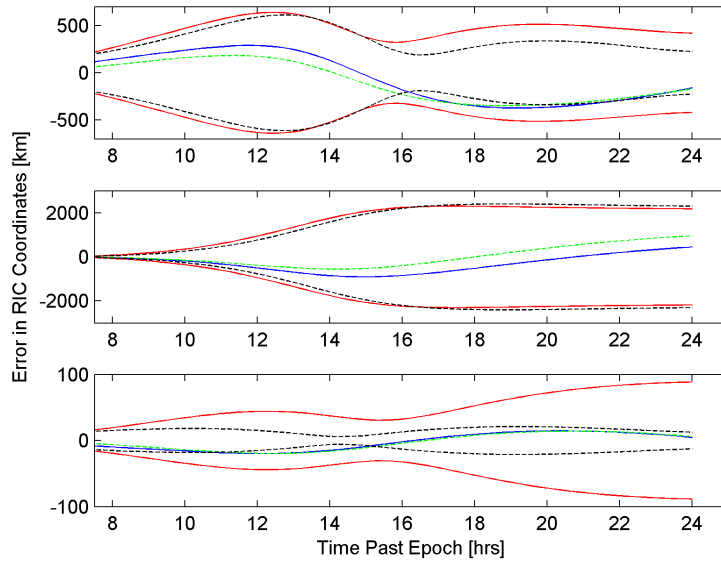


Fig. 6. Estimation error for the MHF and AGM algorithms for the time period starting after the end of the second measurement arc. Estimation error for the AGM is in solid blue and for the MHF is in dashed green. The 3σ estimation error covariance for the AGM is in solid red and for the MHF is in dashed black.

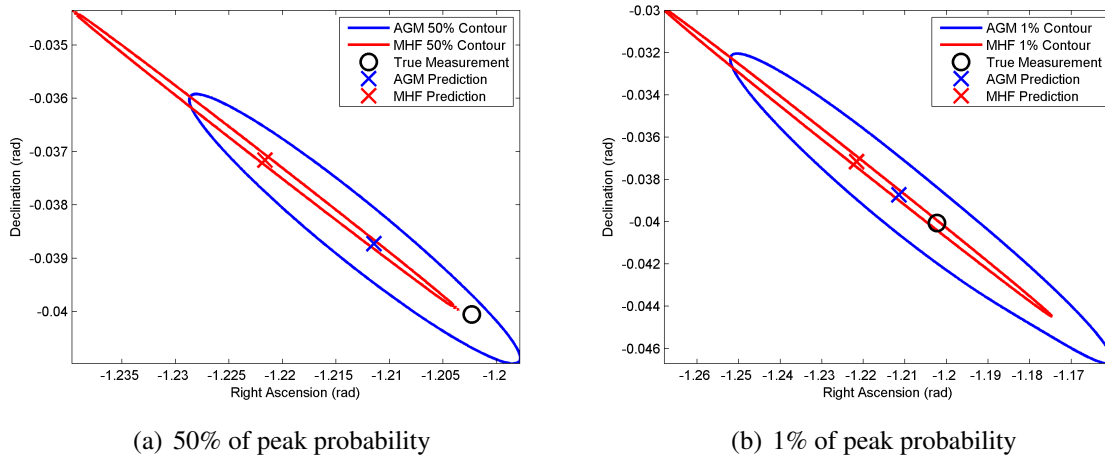


Fig. 7. Final measurement pdf contours. Note: axes are scaled differently to show detail.

for loss of tracking. The implementation of an AGM method to the HAMR object has also been illustrated, showing promise in its ability to more realistically represent the state estimation error knowledge (covariance). Results presented here have shown the following:

- The state error distributions for HAMR RSOs are non-Gaussian.
- A Monte Carlo analysis shows how the state estimation errors exceed the reported uncertainties from the estimation strategy. This clearly shows that the covariances reported are optimistic and if they were to be used for data/track association, could lead to data/track rejections (i.e. false negatives). If there were closely space objects, it could lead to false positives (i.e. the data/track association associates two separate objects believing them to be the same one).

- The AGM confirms a non-Gaussian state estimation error pdf given two significantly weighted components.
- The AGM uncertainties always encompass the state errors (more accurate/realistic than MHF alone).
- The AGM predicted observations are closer to the actual observation than those predicted by the MHF alone (more accurate mean than MHF alone).

These results indicate the potential for allowing reacquisition methods to function more properly due to the more realistic characterization of the uncertainty. As data outages become longer, the need for accurate characterizations of the uncertainties becomes more pressing for the success of followup data association and tracking.

Future work will focus on utilizing the MHF and AGM techniques for identifying the necessary requirements on the angles-only data quality in order to guarantee data/track association and reacquisition of HAMR RSOs. Specific hypotheses to be addressed are as follows:

- An MHF augmented by an AGM is able to better characterize RSOs given poor or unknown a priori information than traditional estimation methods.
- Using an AGM can significantly improve HAMR RSO reacquisition over traditional estimation strategies, especially in the presence of sparse angles-only data.
- For HAMR RSO data/track association and characterization, the quantity of angles-only data can be significantly reduced if fused with temporal photometric signatures
- The AGM is able to significantly aid in HAMR RSO ID/discrimination as compared to traditional estimation strategies.
- The AGM does is better at approximating the true pdf as compared to traditional estimation strategies.
- The more realistic state estimation error distributions produced by AGM improves the realism of conjunction assessments.

In order to guarantee data/track association and reacquisition of HAMR RSOs, the angles-only data quantity, duration and quality required must be analyzed, with sensor noise and biases limited to known performance values. The ultimate goal of new processes that provide improvements to data/track association and conjunction assessment will first be demonstrated via simulation analysis, and eventually, using actual observational data either serendipitously collected, or obtained through coordinated observational experiments.

6. REFERENCES

- [1] Kelecý, T. and M. Jah, "Analysis of Orbit Prediction Accuracy Improvements Using High Fidelity Physical Solar Radiation Pressure Models for Tracking High Area-to-mass Ratio Objects," Fifth European Conference on Space Debris, March 30–April 2, 2009.
- [2] Terejanu, G., J. George and P. Singla, "An Adaptive Gaussian Sum Filter for the Spacecraft Attitude Estimation Problem," AAS 08-262, 2008.
- [3] Vokrouhlický, D., P. Farinella and F. Mignard, "Solar radiation pressure perturbations for Earth satellites: I. A complete theory including penumbra transitions," *Astron. Astrophys.* 280, 295-312, 1993.

- [4] Marshall, J. Andrew and Scott B. Luthke, "Modeling Radiation Forces Acting on Topex/Poseidon for Precision Orbit Determination," *Journal of Spacecraft and Rockets*, Vol. 31, No. 1, January-February 1994.
- [5] Tapley, B., B. Schutz, and G. Born, *Statistical Orbit Determination*, Elsevier Academic Press, New York, NY, 2004.
- [6] Julier, S. and J. Uhlmann, "A New Extension of the Kalman Filter to Nonlinear Systems," *Proceedings of the SPIE - The International Society for Optical Engineering*, Vol. 3068, April 1997, pp. 182–193.
- [7] van der Merwe, R., *Sigma-Point Kalman Filters for Probabilistic Inference in Dynamic State-Space Models*, PhD thesis, Oregon Health and Science University, 2004.
- [8] Escobal, P., *Methods of Orbit Determination*, Krieger Publishing Company, Malabar, FL, 1965.
- [9] Gooding, R., "A New Procedure for Orbit Determination Based on Three Lines of Sight (Angles Only)," Tech. Rep. 93004, Defense Research Agency, 1993.
- [10] DeMars, K., and M. Jah, "Passive Multi-Target Tracking with Application to Orbit Determination for Geosynchronous Objects," AAS Paper 09-108, *19th AAS/AIAA Space Flight Mechanics Meeting*, Savannah, Georgia, February 8–12, 2009.
- [11] Jazwinski, A., *Stochastic Processes and Filtering Theory*, Dover, 2007.
- [12] Risken, H., *The Fokker-Planck Equation: Methods of Solution and Applications*, Springer, 1989.
- [13] Alspach, H. and D. Sorenson, "Nonlinear Bayesian Estimation using Gaussian Sum Approximations," *IEEE Transactions on Automatic Control*, Vol. 17, No. 4, 1972, pp. 439–448.
- [14] Sarkka, S., "On Unscented Kalman Filtering for State Estimation of Continuous-Time Nonlinear Systems," *IEEE Transactions on Automatic Control*, Vol. 55, No. 9, 2007.
- [15] Giza, D., P. Singla, and M. Jah, "An Approach for Nonlinear Uncertainty Propagation: Application to Orbital Mechanics," *AIAA Guidance, Navigation, and Control Conference*, Chicago, Illinois, August 10–13, 2009.
- [16] Honkela, A., "Approximating Nonlinear Transformations of Probability Distributions for Nonlinear Independent Component Analysis," *In IEEE International Joint Conference on Neural Networks*, 2004.
- [17] Kirubarajan, T., Y. Bar-Shalom, W. Blair, and G. Watson, "IMMPDAF for Radar Management and Tracking Benchmark with ECM," *IEEE Transactions on Aerospace and Electronic Systems*, Vol. 34, No. 4, 1998.
- [18] Moyer, T., "Mathematical Formulation of the Double-Precision Orbit Determination Program (DPODP)," Technical Report 32-1527, NASA Jet Propulsion Laboratory, 1971.
- [19] Montenbruck, O. and E. Gill, *Satellite Orbits: Models, Methods, and Applications*, Springer-Verlag, Berlin, 2005.
- [20] Jah, M., E. Graat, D. Highsmith, T. You and E. Higa, "Mars Reconnaissance Orbiter Non-gravitational Force Modeling During Interplanetary Cruise," NASA/JPL Interoffice Memorandum, MRO-NAV-2006-01, January 4, 2006.

DISTRIBUTION LIST

DTIC/OCP 8725 John J. Kingman Rd, Suite 0944 Ft Belvoir, VA 22060-6218	1	cy
AFRL/RVIL Kirtland AFB, NM 87117-5776		2 cy
Moriba Jah Official Record Copy AFRL/RDSM	1	cy